Visualizing Implanted Tumors in Mice with Magnetic Resonance Imaging Using Magnetotactic Bacteria

Michael R. Benoit,[1] Dirk Mayer,[2] Yoram Barak,[1] Ian Y. Chen,[2,3,4] Wei Hu,[5] Zhen Cheng,[2,4] Shan X. Wang,[5] Daniel M. Spielman,[2,4] Sanjiv S. Gambhir,[2,3,4] and A. Matin[1]

Abstract

Purpose: To determine if magnetotactic bacteria can target tumors in mice and provide positive contrast for visualization using magnetic resonance imaging.

Experimental Design: The ability of the magnetotactic bacterium, *Magnetospirillum magneticum* AMB-1 (referred to from here as AMB-1), to confer positive magnetic resonance imaging contrast was determined *in vitro* and *in vivo*. For the latter studies, AMB-1 were injected either i.t. or i.v. Bacterial growth conditions were manipulated to produce small (~25-nm diameter) magnetite particles, which were observed using transmission electron microscopy. Tumor targeting was confirmed using ^{64}Cu-labeled bacteria and positron emission tomography and by determination of viable cell counts recovered from different organs and the tumor.

Results: We show that AMB-1 bacteria with small magnetite particles generate T1-weighted positive contrast, enhancing *in vivo* visualization by magnetic resonance imaging. Following i.v. injection of ^{64}Cu-labeled AMB-1, positron emission tomography imaging revealed increasing colonization of tumors and decreasing infection of organs after 4 hours. Viable cell counts showed that, by day 6, the bacteria had colonized tumors but were cleared completely from other organs. Magnetic resonance imaging showed a 1.22-fold ($P = 0.003$) increased positive contrast in tumors on day 2 and a 1.39-fold increase ($P = 0.0007$) on day 6.

Conclusion: Magnetotactic bacteria can produce positive magnetic resonance imaging contrast and colonize mouse tumor xenografts, providing a potential tool for improved magnetic resonance imaging visualization in preclinical and translational studies to track cancer. (Clin Cancer Res 2009;15(16):5170–7)

Magnetic resonance imaging is a routine diagnostic tool for anatomic and physiologic imaging. Among other applications, magnetic resonance imaging is used to determine the stage of cancer in breast cancer patients (1) and for screening individuals with risk factors for this disease (2). The advantages of magnetic resonance imaging over other imaging techniques include superior (submillimeter) spatial resolution, lack of radiation burden, and unlimited tissue penetration. To enhance *in vivo* image contrast, compounds called contrast agents are often administered to patients. These compounds affect the magnetic resonance imaging signal intensity by locally altering the magnetic field. The effect is to shorten the longitudinal (T1) and transverse (T2) relaxation behavior of surrounding water protons (3), which alters positive (bright) and negative (dark) contrasts, respectively. Contrast agents targeted to specific tissues are desired to serve as probes for help in distinguishing diseased from normal tissue. For *in vivo* imaging, enhancing positive rather than negative contrast is often advantageous because it permits clear distinction from image voids common in anatomic images (4, 5).

A genetically encoded contrast agent capable of targeting cancerous tumors could improve magnetic resonance imaging usefulness in cancer diagnosis and treatment evaluation. Because many bacteria colonize tumors in mice following systemic delivery (6–12), we investigated the magnetic resonance imaging contrast enhancement and tumor targeting ability of *Magnetospirillum magneticum* AMB-1 (referred to from here as AMB-1). AMB-1 produce magnetite (Fe_3O_4) particles (13), which allow them to align along the geomagnetic field of the Earth and find low-oxygen conditions required for their growth (14). We show here that AMB-1 colonize implanted mouse tumors and can be

Authors' Affiliations: Departments of [1]Microbiology and Immunology, [2]Radiology, [3]Bioengineering, [4]Molecular Imaging Program at Stanford, and [5]Department of Materials Science and Engineering, Stanford University, Stanford, California

Received 12/18/08; revised 5/7/09; accepted 5/8/09; published OnlineFirst 8/11/09.

Grant support: *In vivo* Cancer Molecular Imaging Center Program (NIH/National Cancer Institute P50 CA114747; S.S. Gambhir) and grants NIH R01 CA125074-01A1 (A. Matin), NIH RR09784 (D.M. Spielman), and NIH/NIGMS F32GM077827, and NIH T32-AI07328 (M.R. Benoit).

The costs of publication of this article were defrayed in part by the payment of page charges. This article must therefore be hereby marked *advertisement* in accordance with 18 U.S.C. Section 1734 solely to indicate this fact.

Note: Supplementary data for this article are available at Clinical Cancer Research Online (http://clincancerres.aacrjournals.org/).

Current address for Y. Barak: Codexis, Inc., Redwood City, CA 94063.

Requests for reprints: A. Matin, Department of Microbiology and Immunology, 299 Campus Dr., West, Fairchild Sciences Building, Stanford University School of Medicine, Stanford, CA 94305-5124; E-mail: a.matin@stanford.edu.

doi:10.1158/1078-0432.CCR-08-3206

Translational Relevance

This study shows proof-of-principle for generating positive magnetic resonance imaging contrast *in vivo* with bacterial magnetite. *Magnetospirillum magneticum* AMB-1 bacteria might be used directly in translational applications for targeting tumors and enhancing magnetic resonance imaging contrast, although their safe use would need to be shown in humans. Because bacterial magnetite is under genetic control, the potential exists for further translational applications.

manipulated to enhance positive magnetic resonance imaging contrast, providing a useful tool for preclinical studies. Furthermore, the genes responsible for magnetite production might be transferred to mammalian cells to improve magnetic resonance imaging monitoring of cell-based therapies in the clinic.

Materials and Methods

Bacterial strains and growth conditions. AMB-1 (15) was kindly supplied by Dr. Arash Komeili at the University of California, Berkeley. The bacteria were grown at 30°C with modified *Magnetospirillum* growth medium (16). Cultures were grown in sealed tubes with 7% headspace of air. Bacterial cell density was determined by optical density measurements (Shimadzu BioSpec-1601 spectrophotometer) correlated to a standard curve. Iron (40 μmol/L) was supplied either as ferric malate or $FeCl_3$, as described in Results. (*Magnetospirillum* growth medium from here on refers to the medium without supplemental iron.)

Magnetic moment measurements. AMB-1 cells were washed three times and suspended in *Magnetospirillum* growth medium at a range of concentrations. Their magnetic moment was measured with a Princeton MicroMag 2900 alternating gradient magnetometer by applying fields of ±5,000 Oe in 20 Oe steps. Dividing the magnetic moment values by the known magnetic moment of magnetite (480/mL; ref. 17) and multiplying by magnetite density (5.2 g/mL; ref. 18) provided the amount of magnetite per sample. Because 99.5% of iron consumed by magnetotactic bacteria is incorporated into magnetite (19), all cellular iron was assumed to be in magnetite. Iron content is simply the molar ratio (168/232) of iron in magnetite (Fe_3O_4).

Magnetic resonance imaging. For *in vitro* (phantom) studies, AMB-1 samples were washed twice and suspended in 3% gelatin (Sigma G9382) in plastic tubes. Feridex I.V. (Advanced Magnetics, Inc.) phantoms were prepared similarly. The phantoms were aligned inside a 50-mL screw-cap tube, which was subsequently filled with 0.7% agar. The gelatin was snap solidified (4°C) to maintain a homogenous cellular distribution.

For *in vivo* studies, female athymic *nu*$^-$/*nu*$^-$ mice (6-8 wk old; Charles River) were used. S.c. tumors were initiated by injecting 3×10^6 293T human embryonic immortalized kidney cells; this cell line was chosen because it produces firm tumors, permitting i.t. injection. Palpable tumors formed within ~2 wk. Twice washed AMB-1 cells suspended in *Magnetospirillum* growth medium were injected either i.t. at concentrations specified in the Results section or i.v. (tail vein injection) at 1×10^9 cells in 100 μL. For magnetic resonance imaging, animals were anesthetized with isoflurane (2%) plus oxygen (1 L/min) delivered through a nose cone. These studies were done in compliance with a Stanford-approved protocol.

For all magnetic resonance measurements, a GE 3T magnetic resonance scanner equipped with self-shielded gradients (40 mT/m, 150 mT/m/ms) was used. A custom-made radiofrequency quadrature coil was used for radiofrequency excitation and signal reception (Ø = 44 mm for *in vivo* and Ø = 64 mm for *in vitro*). A three-dimensional spoiled gradient recalled (SPGR) sequence (TE/TR = 4/27 ms) with axial slice orientation was used to acquire T1-weighted images over 15 min (nominal resolution, $0.25 \times 0.25 \times 0.5$ mm^3). A two-dimensional gradient recalled echo (GRE) sequence (TE/TR = 9/1,000 ms; 1-mm slice thickness) was used for T2-weighted imaging.

For T1 measurements, an inversion-recovery fast-spin echo sequence (TE/TR = 8.2/10,000 ms; FOV, 64 mm; 128 × 128 matrix; 6-mm slice thickness) was used, with inversion times of 50, 100, 150, 200, 400, 800, 1,500, 2,500, and 4,000 ms. T1 values were estimated by a nonlinear least squares fit of the data to a modified IR curve. A fitting parameter was used to account for the imperfect inversion along the Z axis caused by flip angle deviations due to B_1 inhomogeneities (20). For T2 measurements, an SE sequence was used (TR = 10,000 ms; FOV, 64 mm; 128 × 128 matrix; 6-mm slice thickness) with TEs of 10, 15, 20, 40, 60, 100, 150, 200, 250, and 400 ms. T2 values were estimated by fitting the data to a monoexponential decay curve. Relaxation rate constants ($R_1 = 1/T1$ and $R_2 = 1/T2$) were plotted versus millimole per liter Fe of AMB-1, and the slope was used to determine relaxivity.

Signal intensity was measured from axial-slice 16-bit images using ImageJ (1.39u with the Dicom input/output Plug-in, NIH freeware), background corrected with muscle intensity, and normalized to preinjection values or contralateral controls. Signal intensities were averaged among five consecutive axial-slice images, using mean values from regions of interest (ROI) drawn on the *in vitro* images and maximum values from the *in vivo* images. Maximum values were used for *in vivo* images because of the need to arbitrarily choose ROIs because of localized tumor colonization by AMB-1 following i.t. or i.v. injection. Among the maximum values from five consecutive slices, the SD was consistently <10% of the mean.

Micro–positron emission tomography (PET). ^{64}Cu was produced at the University of Wisconsin by cyclotron irradiation of an enriched ^{64}Ni target according to published methods (21). The ^{64}Cu-pyruvaldehyde-bis(N^4-methylthiosemicarbazone) (PTSM) was prepared as described previously (22). Briefly, the PTSM was prepared by mixing 10 μL of PTSM (dissolved in 1 mg/mL DMSO) with 150 μL of ^{64}Cu (dissolved in 1 mol/L NaOAc; pH 5.5), as described (23). After 3 to 5 min, the mixture was added to an ethanol-preconditioned C-18 SepPak Light column and the ^{64}Cu-PTSM was eluted off with 500 μL ethanol after the first 150 μL fraction.

To optimize labeling conditions, the uptake and efflux of ^{64}Cu-PTSM was examined. For uptake, cells were incubated with 33 μCi for 0.5, 1, 2, 4, and 18 h. At each time point, triplicate samples were washed twice, and activity was counted with a gamma counter. After 2 h, cells had taken up 56.7 ± 2.4% activity, which increased only minimally by 4 h (57.4 ± 2.0%); thus, 2-h incubation was chosen for labeling. For efflux, cells were incubated with 123 μCi for 18 h then resuspended in ice-cold PBS. At 0, 0.5, 2, 4, and 24 h, triplicate samples were pelleted, the supernatant was aspirated, and the activity of the pellet was counted; 24 h later, the samples were found to retain 74.4 ± 2.3% activity. Lack of toxicity of ^{64}Cu-PTSM to AMB-1 cells was verified after 24 h of incubation by microscopic observation of motile cells and by staining with the LIVE/DEAD *Bac*Light viability stain (Molecular Probes).

For the *in vivo* experiment, AMB-1 cells were labeled with ^{64}Cu-PTSM by coincubation for 2 h. 1×10^9 AMB-1 cells suspended in 100 μL (~220 μCi of activity) were injected i.v. through the tail vein to three mice and i.t. to a second group of three mice to serve as positive controls. (1×10^9 cells were used for the positive controls to match the i.v. group, not as a comparison to the i.t. group of the magnetic resonance imaging studies). A third group of mice was injected i.v. with 100 μL of ^{64}Cu-PTSM alone (negative controls). The mice were anesthetized (as described above) and imaged at 0.5, 1, 2, 4, 16, 24, 42, and 64 h postinjection with a Siemens/Concorde Microsystems MicroPET rodent R4. The images were collected with static scans of 3 min (at 0.5, 1, 2, and 4 h), 5 min (at 16 and 24 h), or 10 min (at 42 and 64 h). The microPET images were analyzed using ASIPro VM 6.6.2.0 (Acquisition Sinogram Image PROcessing using the Virtual Machine of IDL). ROIs were drawn

on decay-corrected whole-body coronal images (0.845-mm thickness) and converted to percent injected dose per gram of tissue, as described previously (22). We have previously shown that quantification by this method agrees with biodistribution data (24).

Electron microscopy and size analysis of magnetite particles. Suspensions of AMB-1 were fixed with 2.5% glutaraldehyde in 0.1 mol/L phosphate buffer (pH 7.0) for 1 h, then washed 2× with wash buffer for 10 min. Postfixation was done with 1% osmium tetroxide in fixative buffer for 1 h and rinsed 2× with double-distilled water. The samples were left on 1% uranyl acetate in 20% acetone for 30 min and dehydrated with a graded acetone series. Samples were then infiltrated and embedded in Spurr's resin. Ultrathin sections were cut with a diamond knife and mounted onto uncoated copper grids. The sections were poststained with 2% uranyl acetate for 15 min and 1% lead citrate for 5 min. The samples were examined with a CM-12 Phillips electron microscope. Magnetite particle diameter was measured for >100 magnetite particles per group from digitized transmission electron microscopy (TEM) micrographs using ImageJ 1.39u. The particle diameter histogram was made with 5 nm bins using MATLAB (The Mathworks).

Histology preparation. Tumors were harvested from sacrificed animals and fixed in 10% buffered formalin overnight. Histology preparation was done by Histology Research Core Laboratory at Stanford University Hospital. Slices of 5-mm thickness were embedded in paraffin and longitudinally cut into sections of 5-μm thickness. Neighboring sections were stained with Perl's Prussian blue (for visualizing iron) and Gram stain (for visualizing bacteria), respectively.

Viable plate counts. Nude mice bearing 293T s.c. tumor xenografts were injected with 1×10^9 AMB-1 in 100 μL medium through the tail vein. Groups of three animals were sacrificed 1, 3, and 6 d after injection, and the tumor, liver, and spleen were aseptically removed from each animal. The samples were rinsed with sterile PBS, weighed, and homogenized, then centrifuged at 1,000 rpm for 5 min. Samples from the supernatant were diluted, suspended in 5 mL of warmed *Magnetospirillum* growth medium with 0.7% agar, and plated on *Magnetospirillum* growth medium plates in duplicate. The plates were incubated in bags flushed with N_2 gas at 30°C for 2 wk. Colony forming units were counted and normalized by tissue mass.

Statistical analysis. Two-tailed unpaired *t* tests were done for *in vitro* comparisons, and paired tests were used to compare contrast differences between experimental and control tumors; in paired *t* tests, each tumor was compared with its contralateral control (if applicable) or its own preinjection value. The Mann-Whitney significance test[6] was used to evaluate the difference between distributions (of magnetite particle size or particle number). Statistical significance was determined by $P < 0.05$.

Results

AMB-1 cells generate positive magnetic resonance imaging contrast. Because of the advantage of positive contrast probes for *in vivo* imaging, we focused our investigation on positive contrast enhancement of AMB-1 cells using T1-weighted imaging. AMB-1 cells grown in standard *Magnetospirillum* growth medium (supplemented with ferric malate) failed to generate positive contrast in T1-weighted magnetic resonance images (Fig. 1A, *top row*). We found, however, that if iron in this medium is provided as $FeCl_3$, the bacteria produced positive contrast (Fig. 1A, *bottom row*). The positive contrast was clearly seen at a cell concentration of 0.25×10^{10}/mL and became more intense at 0.5×10^{10}/mL but was reduced by the competing T2 effect (4) at higher concentrations. T1-weighted contrast is quantitatively shown in arbitrary signal intensity units (Fig. 1B) for increasing

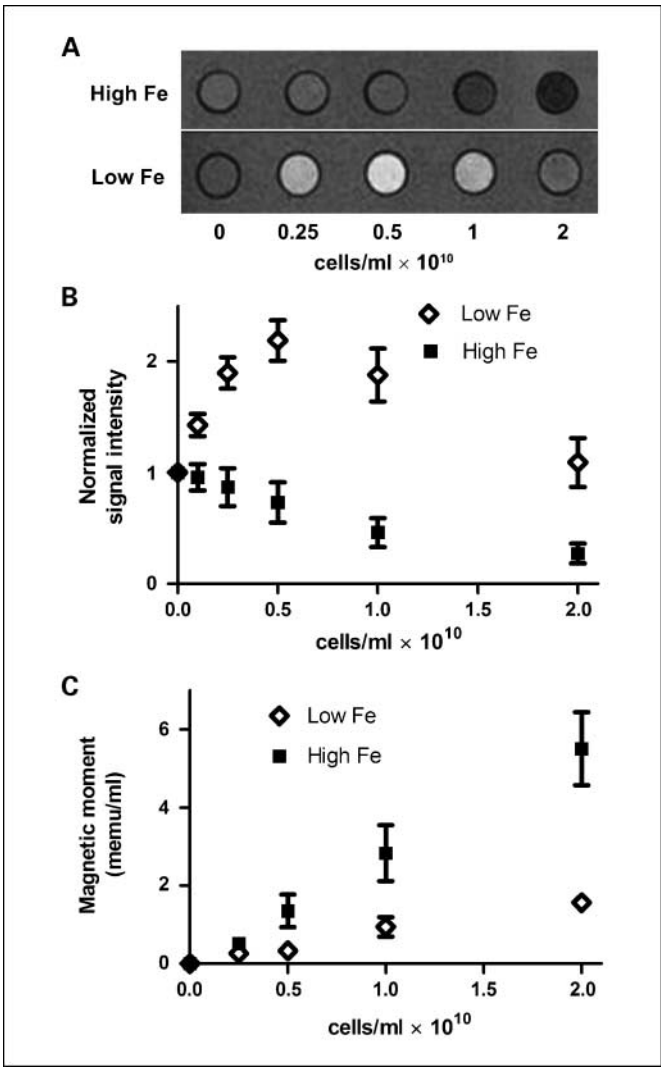

Fig. 1. Contrast enhancement of AMB-1 depends on Fe concentration. *A,* T1-weighted magnetic resonance images show contrast because of AMB-1 cells (at increasing concentrations) grown under high (*top row*)- or low (*bottom row*)-Fe conditions. *B,* mean (±1 SD) normalized signal intensities for AMB-1 cells grown under low (◊)- or high (■)-Fe conditions ($P < 0.05$ at every cell concentration; $n = 3$). *C,* mean (±1 SD) magnetic moments (proportional to magnetite quantity) for AMB-1 grown under low (◊)- or high (■)-Fe conditions.

concentrations of AMB-1 grown with both iron supplements. We also found that cells grown in ferric malate medium possessed higher iron content ($2.2 \pm 0.5 \times 10^{-15}$ g/bacterium) compared with those grown in $FeCl_3$ medium ($0.64 \pm 0.08 \times 10^{-15}$ g/bacterium), as determined by magnetic moment measurements (Fig. 1C). These cells are referred to as "high Fe" and "low Fe," respectively. Note that the low-Fe cells also caused T2-weighted signal loss (Supplementary Fig. S1), permitting their use as either a positive or negative contrast agent.

TEM images revealed that the low-Fe bacteria generated smaller magnetite particles (Fig. 2A) compared with the high-Fe bacteria (Fig. 2B). The median particle diameters under the two conditions were 25.3 and 48.9 nm, respectively, and the particle-diameter distributions (Fig. 2C) were significantly different ($P = 2 \times 10^{-6}$; Mann-Whitney significance test). Despite the difference in particle size, there was no difference in the number of

[6] http://elegans.swmed.edu/~leon/stats/utest.html

magnetite particles per bacterium (6.0 particles for low Fe versus 7.4 for high Fe; $P = 0.14$; Mann-Whitney significance test).

A contrast agent producing a positive signal has relatively high r_1 and low r_2 relaxivities providing a small r_2/r_1 ratio (25). To further characterize the effect of AMB-1 magnetite particle size on magnetic resonance imaging signal properties, we measured r_1 and r_2 of AMB-1 cells with high- and low-Fe content. For low-Fe AMB-1, $r_1 = 9.3$ $(\text{mmol/L})^{-1}\text{s}^{-1}$ and $r_2 = 337$ $(\text{mmol/L})^{-1}\text{s}^{-1}$; for high-Fe AMB-1, $r_1 = 0.68$ $(\text{mmol/L})^{-1}\text{s}^{-1}$ and $r_2 = 48$ $(\text{mmol/L})^{-1}\text{s}^{-1}$. Therefore, the r_2/r_1 ratio of low-Fe AMB-1 ($r_2/r_1 = 36.2$) was smaller than that of high-Fe AMB-1 ($r_2/r_1 = 70.6$), which is consistent with the positive contrast results. We also found that both low- and high-Fe AMB-1 had lower r_2/r_1 ratio than that of Feridex ($r_2/r_1 = 93.7$), the most commonly used iron-oxide contrast agent [$r_1 = 2.7$ $(\text{mmol/L})^{-1}\text{s}^{-1}$ and $r_2 = 253$ $(\text{mmol/L})^{-1}\text{s}^{-1}$].

Positive contrast by AMB-1 cells delivered i.t. To determine if the AMB-1 cells can generate positive contrast *in vivo*, we injected low-Fe AMB-1 cells i.t. in mice implanted with 293T tumor xenografts. Two groups of mice were used. The first group was injected with a range of AMB-1 cells (1.25×10^8 to 5.0×10^8 cells in 50 μL) to determine the correlation between positive contrast and cell concentration *in vivo*. T1-weighted magnetic resonance images showed this correlation in generating positive contrast (Supplementary Fig. S2), consistent with *in vitro* results (Fig. 1). The increased signal was evident immediately following bacterial injection and remained visible one day later. In the second group, two tumor xenografts were

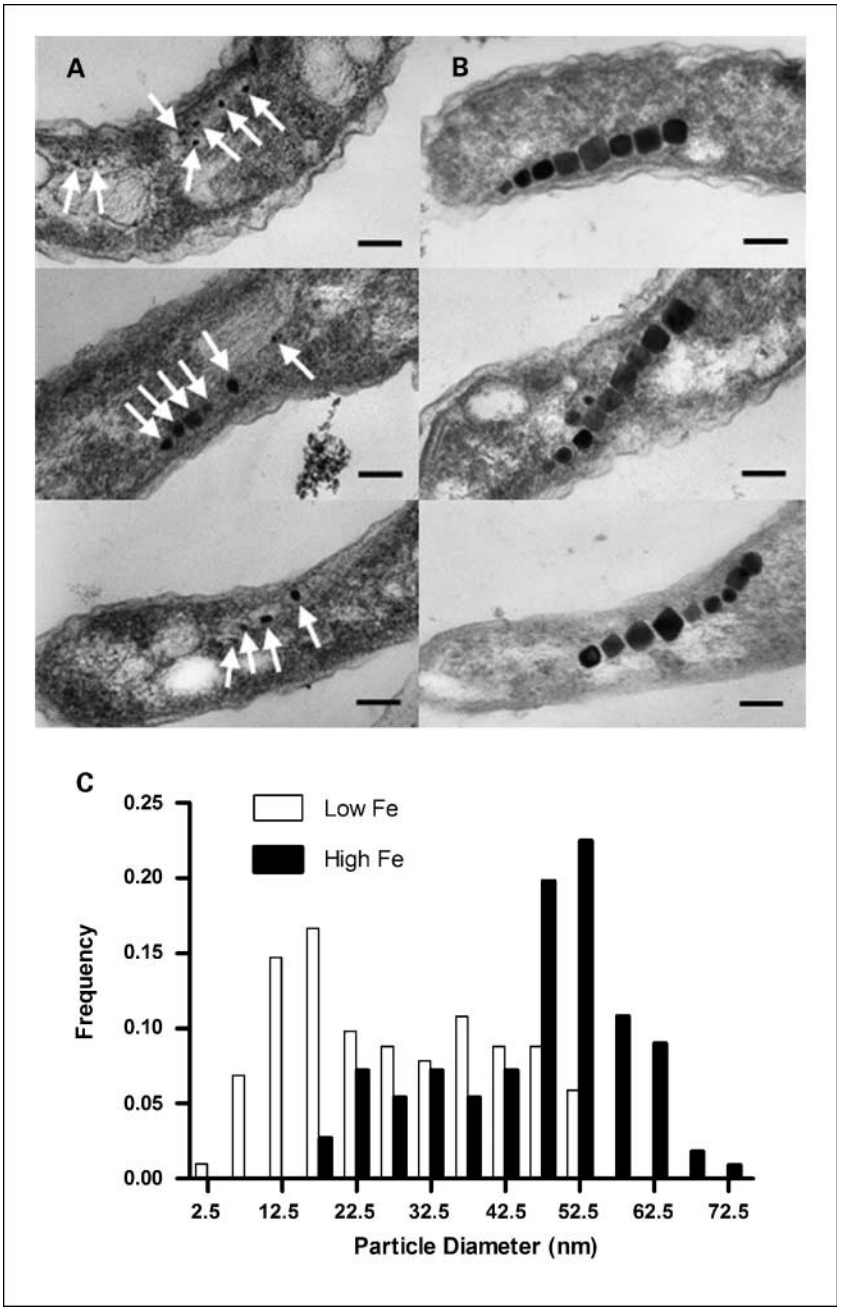

Fig. 2. AMB-1 cells grown with low-Fe have ultrasmall magnetite particles. Representative TEM images of AMB-1 with low (*A*)- or high (*B*)-Fe content. Note the smaller size of magnetite particles in (*A*) versus (*B*). Scale bars, 100 nm; arrows, small magnetite particles. *C*, histogram showing the particle diameter distribution for AMB-1 with low (*white columns*)- or high (*black columns*)-Fe content (frequency is the fraction of particles measured from >100 particles per group).

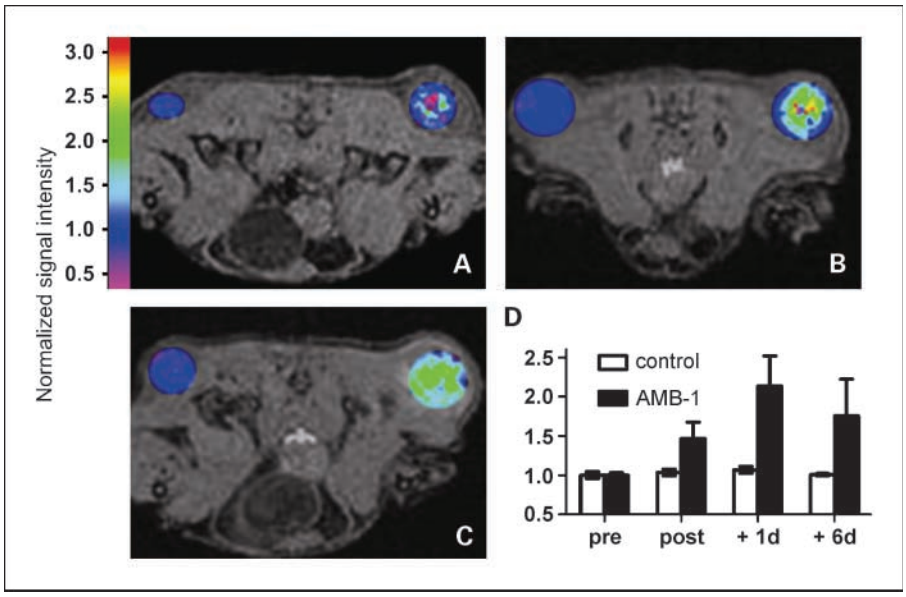

Fig. 3. AMB-1 cells show positive contrast in mouse tumors. T1-weighted axial-slice magnetic resonance images (*A-C*) show enhanced contrast in tumors after i.t. delivery of AMB-1 (*right tumor*) but not in the control tumor injected with *Magnetospirillum* growth medium (*left*): immediately postinjection (*A*), 1 d later (*B*), and 6 d later (*C*). The gradient maps highlight the contrast change at the injection location in the tumor, with the corresponding scale bar illustrating the normalized signal intensity. *D,* mean (±1 SD) tumor signal intensities normalized to preinjection controls for control (*white columns*) or test tumors (*black columns*). Supplementary Fig. S3 shows the magnetic resonance images without the color overlay.

implanted in each mouse, with one serving as a contralateral control (Fig. 3A-C, *left*) injected with 25 μL *Magnetospirillum* growth medium and the other as test tumor (Fig. 3A-C, *right*) injected i.t. with 5×10^8 AMB-1 cells (in 25 μL *Magnetospirillum* growth medium). Following i.t. delivery of AMB-1, the signal intensity increased 1.43-fold immediately ($P = 0.035$; $n = 4$) and 2.02-fold after 1 day ($P = 0.014$; $n = 4$). On day 6, the signal remained clearly visible (Fig. 3C) and 1.77-fold higher

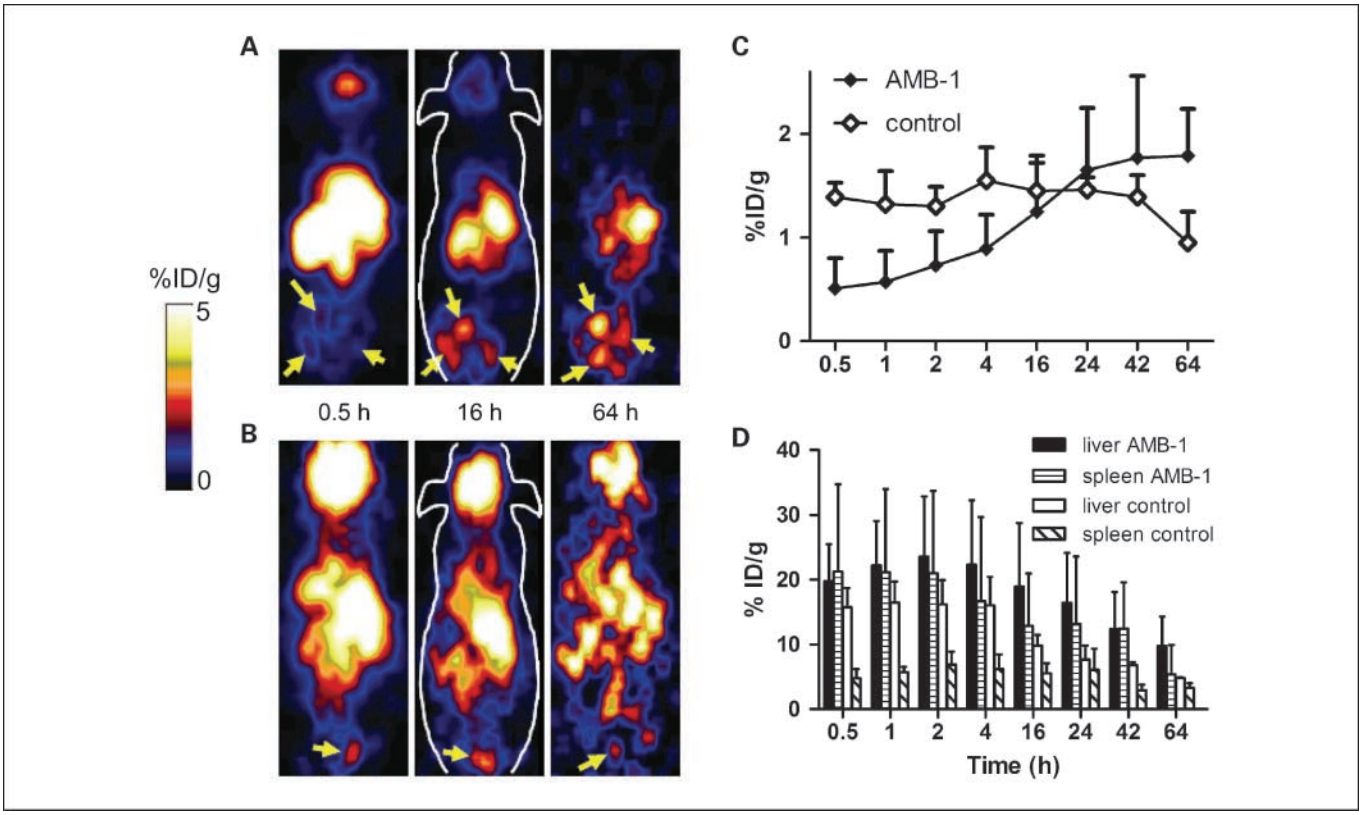

Fig. 4. Biodistribution of ^{64}Cu-PTSM–labeled AMB-1. Decay-corrected, coronal-slice microPET images of mice at indicated times (hour) after i.v. delivery of ^{64}Cu-PTSM–labeled AMB-1 (*A*) or ^{64}Cu-PTSM alone (*B*; negative control). Arrows, hot spots in a single tumor; the color bar, the percentage of the injected dose of ^{64}Cu activity per gram of tissue; an outline of the mouse is traced in the 16-h images for anatomic reference. *C,* mean (±1 SD) signal intensity in tumors showing an increase due to AMB-1 that was not observed in the control group. *D,* in normal tissue (liver and spleen) the mean (±1 SD) signal peaked by 4 h from ^{64}Cu-labeled AMB-1 and ^{64}Cu-PTSM (control) groups. Phagocytosis by spleen macrophages can account for the high percent injected dose per gram of tissue in spleen of the AMB-1 group compared with the control group at early time points.

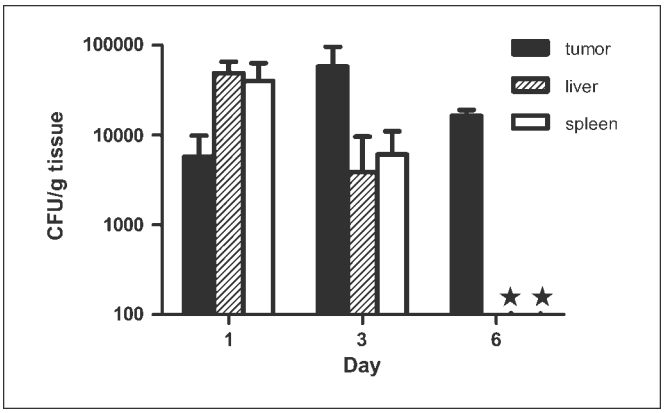

Fig. 5. AMB-1 colonize mouse tumor xenografts following systemic delivery. AMB-1 colony forming units (normalized per gram of tissue) recovered from tail vein–injected nude mice bearing 293T tumor xenografts. Note that no colony forming units were recovered on day 6 from the liver or spleen (★).

than control tumors ($P = 0.10$; $n = 3$). Note that no changes were seen in signal intensities of the control tumors over 6 days (Fig. 3D, *white columns*). On day 7, animals were sacrificed, and their tumor sections were stained with Prussian blue (for iron) and Gram stain (for bacteria). Tumors receiving the bacteria had sections with regions of blue (indicative of iron) coinciding with adjacent sections with spots of red/pink indicative of bacteria (Supplementary Fig. S4); control tumors showed no spots from either stain (not shown).

I.v. delivered AMB-1 cells. For magnetotactic bacteria to provide a useful tool for imaging tumors, they must be capable of colonizing tumors following systemic delivery. We radiolabeled AMB-1 cells with ^{64}Cu-PTSM, which allowed us to examine their detailed biodistribution by the highly sensitive method of PET. Groups of three mice were injected i.v. with labeled bacteria (1×10^9 cells) or ^{64}Cu-PTSM (negative control) or injected i.t. with labeled bacteria (positive control). PET images were obtained at eight time points between 0.5 and 64 hours postinjection. After i.t. injection (positive control group), the ^{64}Cu signal remained largely confined to the tumor for 64 hours (Supplementary Fig. S5). Shortly after i.v. injection (0.5 hour), radioactivity (percent injected dose per gram of tissue) was found primarily in highly vascularized regions like the liver and spleen (Fig. 4A). Note that little radioactivity is seen in the brain of animals injected with the labeled bacteria (Fig. 4A) as opposed to the negative controls (Fig. 4B). Because bacteria cannot typically cross the blood-brain barrier, this verifies that ^{64}Cu-PTSM was largely retained in the labeled AMB-1 cells *in vivo*. In fact, the signal in the brains of the AMB-1 injected group at 0.5 hour (1.2 %ID/g) was 16.7% of that in the control group (7.2 %ID/g), agreeing closely with *in vitro* ^{64}Cu-PTSM efflux from AMB-1 of 17.6% after 0.5 hour (not shown). In the tumor, the PET signal up to the first 16 hours is higher in the control animals directly receiving ^{64}Cu-PTSM i.v. compared with the test animals injected with ^{64}Cu-labeled bacteria, most likely because of the porous nature of tumor vasculature. The tumor vasculature is expected to permit rapid diffusion of ^{64}Cu-PTSM into the tumor but slower penetration of micron-sized bacteria. The relevant point is the trend of increasing signal in the test tumors (Fig. 4C), which had a higher signal after 64 hours compared with 0.5 hour ($P = 0.020$). In control tumors, the signal began to decrease after 4 hours (Fig. 4C), which was also the case for normal tissue (liver and spleen) in both the control and test animals (Fig. 4D). This trend strongly suggests that the labeled bacteria accumulated in the tumor over the course of the experiment.

Because of the short half-life of ^{64}Cu (12.7 hours), we did a separate experiment with viable counts to investigate the distribution of AMB-1 for >64 hours. Groups of three mice bearing 293T tumor xenografts were i.v. injected with 1×10^9 AMB-1 through the tail vein. After 1, 3, and 6 days, groups of animals were sacrificed; the tumors, livers, and spleens were harvested, weighed, and homogenized; and samples were plated for colony forming units. One day postinjection, the number of colony forming units recovered was higher in liver and spleen compared with the tumor. This trend reversed by day 3, and by day 6, no viable bacteria were found in liver or spleen; they were found only in tumor (Fig. 5).

To determine the magnetic resonance imaging signal progression following i.v. AMB-1 administration, a group of four mice bearing 293T tumors were injected with low-Fe AMB-1 through the tail vein. T1-weighted images were collected before injection as well as 2 and 6 days postinjection. The signal increased 1.22-fold ($P = 0.003$) after 2 days and 1.39-fold ($P = 0.0007$) after 6 days (Fig. 6). Following the experiment, tumor sections stained with Prussian blue indicated the presence of iron for mice injected with AMB-1 but not for control animals (not shown). An independent experiment in which the images were

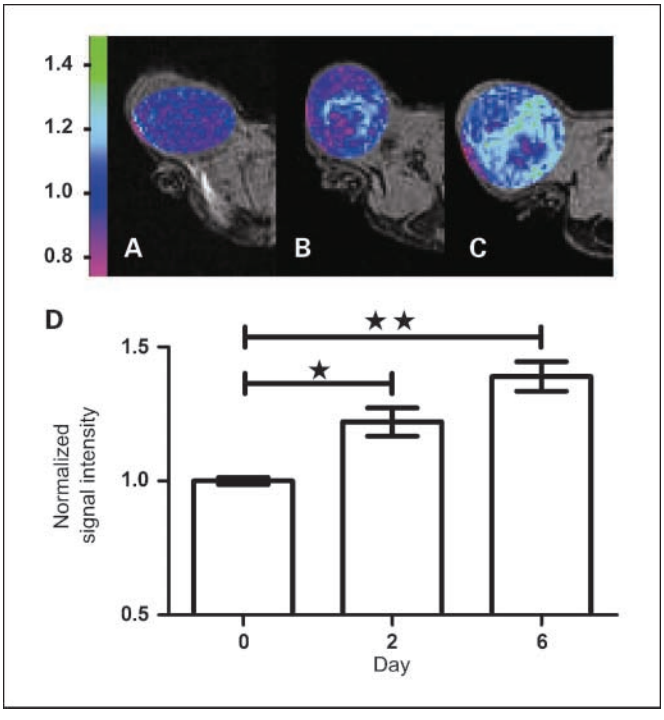

Fig. 6. AMB-1 produce positive contrast in tumor xenografts following systemic delivery. T1-weighted, axial-slice magnetic resonance images of a mouse tumor before injection (*A*) as well as 2 (*B*) and 6 d postinjection (through tail vein with 1×10^9 AMB-1 suspended in 100 μL *Magnetospirillum* growth medium). The color column shows normalized signal intensity within the gradient maps. *D*, the signal increased 1.22-fold (★ $P = 0.003$) after 2 d and 1.39-fold (★★ $P = 0.0007$) after 6 d ($n = 4$). Supplementary Fig. S6 shows the magnetic resonance images without the color overlay.

acquired only on day 6 also showed 1.43 (±0.12)-fold ($P = 0.001$; $n = 5$) increase in signal compared with controls (not shown).

Discussion

We show here that the magnetotactic bacterium AMB-1 can generate either positive (T1 weighted) or negative (T2 weighted) magnetic resonance imaging contrast *in vitro*. Positive contrast was visible for AMB-1 grown with $FeCl_3$ supplemented medium but not for AMB-1 grown in standard *Magnetospirillum* growth medium (supplemented with ferric malate). The positive contrast producing AMB-1 had low Fe content, and TEM images revealed that the low-Fe AMB-1 possessed magnetite particles with smaller median diameter (25.3 versus 48.9 nm). We attribute this to reduced iron solubility of $FeCl_3$ in the growth medium compared with ferric malate. With respect to particle size, the magnetite particles resemble superparamagnetic iron oxides, in that larger particles (60-150 nm) do not produce positive contrast (3), whereas recent reports describe the use of ultrasmall superparamagnetic iron oxide particles (10-40 nm) for positive contrast enhancement (25–29). Note that the median particle diameter in our low-Fe bacteria was 25.3 nm, which is midrange for ultrasmall superparamagnetic iron oxide particle size.

Positive contrast was also visible in tumor xenografts following direct injection of low-Fe AMB-1. Thus, magnetotactic bacteria can potentially act as positive contrast enhancing agents in magnetic resonance imaging *in vivo*. But whether they can be used as an experimental probe in magnetic resonance imaging–based cancer visualization in preclinical models depends also on their ability to target tumors. We show, using several approaches (PET, viable counts, and magnetic resonance imaging), that this is indeed the case. The viable counts suggest continued accumulation and/or multiplication of AMB-1 in the tumors. These findings agree with published reports of tumor colonization and multiplication by other bacteria, which for example, showed peak titers on day 4 followed by a decline to day 12 (10). Our PET images showed increasing amounts of ^{64}Cu in tumors, indicating that at least part of the increase in AMB-1 between days 1 and 3 is due to continued accumulation of AMB-1 in the tumor. However, it is possible that their multiplication also contributed because we found that AMB-1 multiplied and formed magnetite at 37°C *in vitro* (not shown). Regardless, 2 and 6 days after i.v. delivery, AMB-1 produced clearly visible positive magnetic resonance imaging contrast in tumors. Thus, this proof-of-principle study is the first to show that magnetotactic bacteria delivered i.v. can accumulate in tumors and visibly increase magnetic resonance imaging signal.

For translational applications of these findings, it is desirable to transfer the essential magnetite-forming genes to suitable mammalian delivery agents. For instance, cytokine-induced killer cells can track cancer as they naturally target tumors and also act as therapeutic agents (30). Similarly, stem cells can be used to track stem cell therapy (31). Recently, it was shown that a single gene may be sufficient to generate T2-weighted negative contrast in an immortalized mammalian cell line (32). We are currently determining the genes needed to generate magnetite particles in primary mammalian cells as well as whether the four genes that control magnetite particle size in magnetotactic bacteria (33) can play the same role in mammalian cells (to generate small particles for positive contrast). We also note that the capacity to direct magnetite to tumors has direct applications in therapies such as hyperthermia, in which external magnetic fields are applied to generate heat and kill tumor cells (34).

Disclosure of Potential Conflicts of Interest

No potential conflicts of interest were disclosed.

Acknowledgments

We thank Dr. Shay Keren and Dr. Robert Wilson for the fruitful discussions, and Anne Sawyer, Sandra Rodriguez, Romi Samra, Julia Rasooly, Nafisa Ghori, Dr. Jennifer Prescher, Dr. Zhe Liu, Dr. Laura Pisani, and Dr. Guangchao Li for the technical assistance.

References

1. Margolis DJ, Hoffman JM, Herfkens RJ, Jeffrey RB, Quon A, Gambhir SS. Molecular imaging techniques in body imaging. Radiology 2007; 245:333–56.
2. Kriege M, Brekelmans CT, Boetes C, et al. Efficacy of MRI and mammography for breast-cancer screening in women with a familial or genetic predisposition. N Engl J Med 2004;351:427–37.
3. Thorek DL, Chen AK, Czupryna J, Tsourkas A. Superparamagnetic iron oxide nanoparticle probes for molecular imaging. Ann Biomed Eng 2006;34:23–38.
4. Cunningham CH, Arai T, Yang PC, McConnell MV, Pauly JM, Conolly SM. Positive contrast magnetic resonance imaging of cells labeled with magnetic nanoparticles. Magn Reson Med 2005;53:999–1005.
5. Mani V, Briley-Saebo KC, Itskovich VV, Samber DD, Fayad ZA. Gradient echo acquisition for superparamagnetic particles with positive contrast (GRASP): sequence characterization in membrane and glass superparamagnetic iron oxide phantoms at 1.5T and 3T. Magn Reson Med 2006;55:126–35.
6. Brown JM, Wilson WR. Exploiting tumour hypoxia in cancer treatment. Nat Rev Cancer 2004;4: 437–47.
7. Dang LH, Bettegowda C, Huso DL, Kinzler KW, Vogelstein B. Combination bacteriolytic therapy for the treatment of experimental tumors. Proc Natl Acad Sci U S A 2001;98:15155–60.
8. Kasinskas RW, Forbes NS. *Salmonella typhimurium* lacking ribose chemoreceptors localize in tumor quiescence and induce apoptosis. Cancer Res 2007;67:3201–9.
9. Liu SC, Minton NP, Giaccia AJ, Brown JM. Anticancer efficacy of systemically delivered anaerobic bacteria as gene therapy vectors targeting tumor hypoxia/necrosis. Gene Ther 2002;9:291–6.
10. Min JJ, Nguyen VH, Kim HJ, Hong Y, Choy HE. Quantitative bioluminescence imaging of tumor-targeting bacteria in living animals. Nat Protoc 2008;3:629–36.
11. Soghomonyan SA, Doubrovin M, Pike J, et al. Positron emission tomography (PET) imaging of tumor-localized *Salmonella* expressing HSV1-TK. Cancer Gene Ther 2005;12:101–8.
12. Zhao M, Geller J, Ma H, Yang M, Penman S, Hoffman RM. Monotherapy with a tumor-targeting mutant of *Salmonella typhimurium* cures orthotopic metastatic mouse models of human prostate cancer. Proc Natl Acad Sci U S A 2007; 104:10170–4.
13. Bazylinski DA, Frankel RB. Magnetosome formation in prokaryotes. Nat Rev Microbiol 2004;2: 217–30.
14. Smith MJ, Sheehan PE, Perry LL, et al. Quantifying the magnetic advantage in magnetotaxis. Biophys J 2006;91:1098–107.
15. Matsunaga T, Sakaguchi T, Tadokoro F. Magnetite formation by a magnetic bacterium capable of growing aerobically. Appl Microbiol Biotechnol 1991;35:651–5.
16. Komeili A, Vali H, Beveridge TJ, Newman DK. Magnetosome vesicles are present before magnetite formation, and MamA is required for their activation. Proc Natl Acad Sci U S A 2004;101: 3839–44.
17. Cullity BD. Introduction to magnetic materials. 2nd ed. Hoboken (NJ): IEEE Press, Wiley; 2009.
18. Windholz M, Budavari S, Blumetti RF, Otterbein ES.TheMerckindex.10thed:Merck&Co.,Inc.;1983.

19. Grunberg K, Muller EC, Otto A, et al. Biochemical and proteomic analysis of the magnetosome membrane in *Magnetospirillum gryphiswaldense*. Appl Environ Microbiol 2004;70:1040–50.

20. Rakow-Penner R, Daniel B, Yu H, Sawyer-Glover A, Glover GH. Relaxation times of breast tissue at 1.5T and 3T measured using IDEAL. J Magn Reson Imaging 2006;23:87–91.

21. Avila-Rodriguez MA, Nye JA, Nickles RJ. Simultaneous production of high specific activity 64Cu and 61Co with 11.4 MeV protons on enriched 64Ni nuclei. Appl Radiat Isot 2007;65:1115–20.

22. Adonai N, Nguyen KN, Walsh J, et al. *Ex vivo* cell labeling with 64Cu-pyruvaldehyde-bis(*N*4-methylthiosemicarbazone) for imaging cell trafficking in mice with positron-emission tomography. Proc Natl Acad Sci U S A 2002;99:3030–5.

23. Blower PJ, Lewis JS, Zweit J. Copper radionuclides and radiopharmaceuticals in nuclear medicine. Nucl Med Biol 1996;23:957–80.

24. Cheng Z, Xiong Z, Subbarayan M, Chen X, Gambhir SS. 64Cu-labeled α-melanocyte-stimulating hormone analog for microPET imaging of melanocortin 1 receptor expression. Bioconjug Chem 2007;18:765–72.

25. Kellar KE, Fujii DK, Gunther WH, et al. NC100150 injection, a preparation of optimized iron oxide nanoparticles for positive-contrast MR angiography. J Magn Reson Imaging 2000;11:488–94.

26. Baio G, Fabbi M, de Totero D, et al. Magnetic resonance imaging at 1.5 T with immunospecific contrast agent *in vitro* and *in vivo* in a xenotransplant model. MAGMA 2006;19:313–20.

27. Jander S, Schroeter M, Saleh A. Imaging inflammation in acute brain ischemia. Stroke 2007;38:642–5.

28. Lutz AM, Weishaupt D, Persohn E, et al. Imaging of macrophages in soft-tissue infection in rats: relationship between ultrasmall superparamagnetic iron oxide dose and MR signal characteristics. Radiology 2005;234:765–75.

29. Pouliquen D, Perroud H, Calza F, Jallet P, Le Jeune JJ. Investigation of the magnetic properties of iron oxide nanoparticles used as contrast agent for MRI. Magn Reson Med 1992;24:75–84.

30. Edinger M, Cao YA, Verneris MR, Bachmann MH, Contag CH, Negrin RS. Revealing lymphoma growth and the efficacy of immune cell therapies using *in vivo* bioluminescence imaging. Blood 2003;101:640–8.

31. Chapon C, Jackson JS, Aboagye EO, Herlihy AH, Jones WA, Bhakoo KK. An *in vivo* multimodal imaging study using MRI and PET of stem cell transplantation after myocardial infarction in rats. Mol Imaging Biol 2008.

32. Zurkiya O, Chan AW, Hu X. MagA is sufficient for producing magnetic nanoparticles in mammalian cells, making it an MRI reporter. Magn Reson Med 2008;59:1225–31.

33. Scheffel A, Gardes A, Grunberg K, Wanner G, Schuler D. The major magnetosome proteins MamGFDC are not essential for magnetite biomineralization in *Magnetospirillum gryphiswaldense* but regulate the size of magnetosome crystals. J Bacteriol 2008;190:377–86.

34. Moroz P, Jones SK, Winter J, Gray BN. Targeting liver tumors with hyperthermia: ferromagnetic embolization in a rabbit liver tumor model. J Surg Oncol 2001;78:22–9. discussion 30-1.